Synthesis, Structural, Textural, Optical, Photoluminescence, and Magnetic Properties of $Co_{0.21}Cu_{0.79}O$ Nanoparticles Fabricated through $[Co_{0.21}Cu_{0.79}(Cre)_2(N_2H_4)_2]$ Precursor. Evaluation of *In Vitro* Antioxidant and Anticancer Activities

N. Anjuthaprabha, R. Manimekalai

Department of Chemistry, Kongunadu Arts and Science College, Coimbatore, Tamil Nadu, India

Abstract

We fabricated $Co_{0.21}Cu_{0.79}O$ nanoparticles from co-precipitation followed by thermal decomposition of cobalt doped copper creatinate hydrazinate ($[Co_{0.21}Cu_{0.79}(Cre)_2(N_2H_4)_2]$) inorganic precursor. The inorganic precursor was characterized through energy dispersive X-ray spectroscopy (EDS), Inductively Coupled Plasma Atomic Emission Spectrophotometry (ICP-AES), Fourier transform infrared (FT-IR), and thermogravimetry-differential thermal analyser analysis. To characterize the composition, structural phase, chemical state, morphological, and textural properties of fabricated $Co_{0.21}Cu_{0.79}O$ nanoparticles techniques such as EDS, ICP-AES, X-ray diffraction, FT-IR, Raman, X-ray photoelectron spectroscopy, Scanning electron microscopy, transmission electron microscope, and Brunauer–Emmett–Teller were used. The *in vitro* antioxidant activity of $Co_{0.21}Cu_{0.79}O$ nanoparticles was assessed by 2,2-diphenyl-1-picryl-hydrazyl-hydrate free radical assay. Furthermore, the *in vitro* cytotoxic activity of $Co_{0.21}Cu_{0.79}O$ nanoparticles was evaluated against human embryonic kidney 293 and HeLa cell lines using 3-[4,5-dimethylthiazol-2-yl]2,5-diphenyltetrazolium bromide assay.

Keywords: Nanoparticles, Creatinate, Co-precipitation, Thermal decomposition, Characterization, *In vitro* antioxidant, *In vitro* cytotoxicity.

1. INTRODUCTION

Copper oxide (CuO) nanoparticles are gaining interest because of their wealthy advantages. CuO with variety of metal combinations was reported earlier. Among them, transition metals doped CuO are fascinating. In the line, Co-doped CuO nanoparticles were prepared with different ratios by various techniques such as sol-gel [1,2], microwave-assisted [3,4], solvothermal microwave irradiation [5], wet chemical [6], and co-precipitation [7,8]. Besides Co-doped CuO nanoparticles having advantages in an optical, magnetic, and electrical field, they have applications in the biological field [3,9] too. Moreover, hydrazine can bind with metals and acids to form complexes. The hydrazine complexes have been used as precursors for metal and mixed metal oxide nanoparticles [10-20]. In this chapter, we discussed the preparation of $Co_{0.21}Cu_{0.79}O$ nanoparticles through co-precipitation followed by thermal decomposition technique from its hydrazine precursor. The structural, textural, optical, and magnetic properties of prepared $Co_{0.21}Cu_{0.79}O$ nanoparticles are discussed in detail. Further, in this chapter, we discuss the *in vitro* biological activities of $Co_{0.21}Cu_{0.79}O$ nanoparticles.

2. EXPERIMENTAL SECTION

2.1. Preparation of $[Co_{0.21}Cu_{0.79}(Cre)_2(N_2H_4)_2]$, Where Cre-Creatinate $(H_2NC(=NH)N(CH_3)CH_2COO^-)_2$

The precursor $[Co_{0.21}Cu_{0.79}(Cre)_2(N_2H_4)_2]$ was prepared by the addition of an aqueous solution (50 mL) of hydrazine hydrate (2.0 mL, 0.0399 mol) and creatine monohydrate (2.0 g, 0.0134 mol) to the corresponding aqueous solution (50 mL) of $Cu(NO_3)_2.3H_2O$ (0.79 g, 0.00326 mol)

and $Co(NO_3)_2.6H_2O$ (0.21 g, 0.00072 mol) was added drop wise with constant stirring. A dark brown colored precipitate was formed in a few minutes. The obtained reaction mixture was kept aside for 1 h, and then filtered. The precipitate washed with water, ethanol followed by diethyl ether to remove adsorbed impurities and then dried at room temperature.

Yield: 4.1 g (81%)

Melting point: 216°C

$$0.21Co(NO_3)_2.nH_2O + 0.79Cu(NO_3)_2.nH_2O +$$
$$2(H_2NC(=NH)N(CH_3)CH_2COOH).H_2O + 2N_2H_4.H_2O$$
$$\downarrow aqueous\ solution$$
$$[Co_{0.21}Cu_{0.79} + (H_2NC(=NH)N(CH_3)CH_2COO)_2(N_2H_4)_2$$
$$+2HNO_3 + nH_2O \tag{1}$$
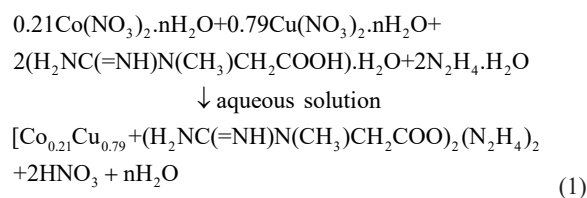
2.2. Synthesis of $Co_{0.21}Cu_{0.79}O$ Nanoparticles

This method involves transferring of the dried cobalt doped copper creatinate hydrazinate ($[Co_{0.21}Cu_{0.79}(Cre)_2(N_2H_4)_2]$) inorganic

*Corresponding author:
Email: rmanimekalai04@gmail.com

precursor to a silica crucible and calcined in a muffle furnace at 250°C for 30 min resulting in the formation of fine black $Co_{0.21}Cu_{0.79}O$ nanoparticles (as prepared). The heating source was then removed; the product was allowed to cool at room temperature and then stored in airtight containers.

$$[Co_{0.21}Cu_{0.79}(H_2NC(=NH)N(CH_3)CH_2COO)_2(N_2H_4)_2]+25O_2$$
$$\Delta \downarrow 250°C$$
$$Co_{0.21}Cu_{0.79}O+8CO_2+5N_2+12H_2O \tag{2}$$
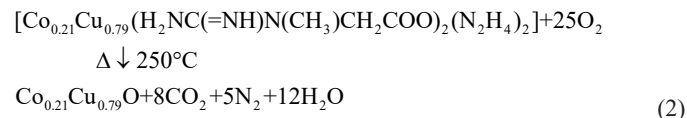
3. CHARACTERIZATION TECHNIQUES

The hydrazine content in the precursor was determined by titration using KIO_3 as titrant under Andrew's conditions[30]. Elemental analysis was performed on an Elementar Vario EL III CHN analyzer at digestion temperature in the range of 950–1200°CC. The Fourier transform infrared (FT-IR) spectra of the solid sample were recorded on an FT-IR spectrophotometer (Shimadzu Prestige-21series) in the spectral range of 4000-400 cm^{-1} using KBr pellets. Differential scanning calorimetry (DSC) measurement of finely powdered sample was performed using a Mettler Toledo DSC 822e. DSC calorimeter at a heating rate of 20°C·min^{-1} in the temperature ranges at RT-700°C. Thermogravimetric (TGA) experiment was carried out using a Perkin Elmer, STA-6000, at a heating rate of 20 °C·min^{-1} in the temperature range RT-700°C. Platinum cups were used as sample holders and alumina as a reference. Inductively Coupled Plasma Atomic Emission Spectrophotometry (ICP-AES) of the solid sample was recorded by atomic emission spectrometer (Thermo Electron IRIS INTREPID II XSP DUO). X-ray diffraction (XRD) pattern of the oxide sample was recorded using Shimadzu XRD 6000 diffractometer at room temperature, with the mean Cukα radiation ($\lambda = 1.5418$ Å) at a voltage of 40.0 (kV) and a current of 30.0 (mA), between 10° (2θ) and 90°(2θ) with a sampling pitch of 1° in a continuous scan mode and a speed of 10°/min. Raman spectra were recorded using Bruker RFS 27 with laser source is Nd: YAG 1064 nm. X-ray photoelectron spectroscopy (XPS) measurement of a product was conducted using an Omicron ESCA probe spectrometer with monochromatized Al Kα X-rays (1486.6eV). The transmission electron microscope (TEM) micrograph of oxide sample was taken using Jeol/JEM 2100 electron microscope at an accelerating voltage of 200kV. Scanning electron microscopy (SEM) was performed with a Hitachi Model S-3000H by focusing on nanoparticles to study morphology. Brunauer-Emmett-Teller (BET) surface area was performed on Quantachrome autosorb automated gas sorption system. An optical analysis was performed with a UV-Vis spectrophotometer (Varian, Cary 5000, spectral range 175–800 nm). Photoluminescence (PL) characterization of the oxide sample was carried out by Fluromax-4 spectrometer in which Xenon is used as the source. The magnetic measurement of the oxide sample was performed at room temperature by a vibrating sample magnetometer (Lakeshore VSM 7410).

4. BIOLOGICAL ACTIVITIES

4.1. In Vitro 2,2-Diphenyl-1-picryl-hydrazyl-hydrate (DPPH) Scavenging Activity

The hydrogen donating ability of the sample was examined in the presence of DPPH stable radical [21]. In the present work, using some modification in the DPPH method [22], we assessed the antioxidant activity of nanoparticles. 1 mL of 0.3 mM DPPH methanol solution was added to 1 mL of different concentration the nanoparticles (10, 20 40, 60, 80, and 100 µg/mL). The mixture was allowed for sonication to enhance the reaction between insoluble nanoparticles and the DDPH reagent and kept in the dark at room temperature for 30 min

and centrifuged, the supernatant was collected and the absorbance values were measured at 517 nm. The methanol solution was used as a blank and DPPH solution (1 mL, 0.3mM) with 1mL methanol served as a negative control. Ascorbic acid was taken as a positive control. A control reaction was carried without the test sample. The mean values were obtained from the triplicate analysis. The percentage of inhibition was calculated by comparing the absorbance values of the control and test samples.

$$\text{DDPH scavenging activity (\%)} = AC - A_{\text{test sample}}/AC \times 100 \tag{3}$$

Where A_C was the absorbance of the control reaction and $A_{\text{test sample}}$ was the absorbance in the presence of a test sample. For determining IC_{50} (the number of samples required to scavenge 50% of DPPH), a similar procedure is adopted with 10, 20, 40, 60, 80, and 100 µg/mL of the nanoparticles and absorbance's were recorded after 30 min.

4.2. In Vitro Assay for Cytotoxic Activity (3-[4,5-Dimethylthiazol-2-yl]2,5-diphenyltetrazolium bromide[MTT] Assay)

The human embryonic kidney normal cell (HEK 293) and human cervical cancer cells (HeLa were obtained from National Centre for Cell Science, Pune and grown in Eagles Minimum Essential Medium containing 10% fetal bovine serum (FBS). The cell was maintained at 37°C, 5% CO2, 95% air, and 100% relative humidity. Maintenance cultures were passaged weekly, and the culture medium was changed twice a week. The monolayer cells were detached with trypsin-ethylenediaminetetraacetic acid to make single-cell suspensions and viable cells were counted using a hemocytometer and diluted with a medium containing 5% FBS to give a final density of 1×10^5 cells/ml. One hundred microliters per well of cell suspension were seeded into 96-well plates at a plating density of 10,000 cells/well and incubated to allow for cell attachment at 37°C, 5% CO2, 95% air, and 100% relative humidity. After 24 h, the cells were treated with serial concentrations of the test samples (nanoparticles). They were initially dispersed in phosphate-buffered saline (PBS) by sonication and an aliquot of the sample solution was diluted to twice the desired final maximum test concentration with a serum-free medium. Additional four serial dilutions were made to provide a total of five sample concentrations. Aliquots of 100 µl of these different sample dilutions were added to the appropriate wells already containing 100 µl of the medium, resulting in the required final sample concentrations. Following sample addition, the plates were incubated for an additional 48 h at 37°C, 5% CO2, 95% air, and 100% relative humidity. The medium containing without samples were served as control and triplicate were maintained for all concentrations.

4.2.1. MTT assay

MTT is a yellow water-soluble tetrazolium salt. A mitochondrial enzyme in living cells, succinate-dehydrogenase, cleaves the tetrazolium ring, converting the MTT to an insoluble purple formazan. Therefore, the amount of formazan produced is directly proportional to the number of viable cells.

After 48 h of incubation, 15 µl of MTT (5 mg/ml) in PBS was added to each well and incubated at 37^vC for 4 h. The medium with MTT was then flicked off and the formed formazan crystals were solubilized in 100 µl of DMSO and then measured the absorbance at 570 nm using a microplate reader. The % cell inhibition was determined using the following formula [23,24],

$$\text{\% Cell inhibition} = 100 - Abs_{\text{sample}}/Abs_{\text{control}} \times 100 \tag{4}$$

A nonlinear regression graph was plotted between % Cell inhibition and Log concentration and IC50 was determined using GraphPad Prism software.

4.3. Reactive Oxygen Species (ROS) Analysis

For quantitative ROS analysis, cells (1×10^5 per well) were seeded in black bottom 96-well culture plate and incubated for 24 h in a CO_2 incubator at 37°C. HEK 293 and HeLa cells were treated with different concentrations (6.25 μg/ml–100 μg/ml) of nanoparticles for 12 h. After exposure, the cells were incubated with DCFH-DA (10 mM) for 30 min at 37°C. Fluorescence intensity was measured at excitation and emission wavelength of 485 and 528 nm, respectively. Values were expressed as the percentage of fluorescence intensity relative to the control wells [25].

5. RESULTS AND DISCUSSION

5.1. Characterization of the Precursor

5.1.1. Analytical data

The hydrazine content in the precursor was determined by titration using KIO_3 as titrant under Andrew's conditions [26]. The Energy Dispersive X-Ray Spectroscopy (EDS) spectra (Figure 1a) confirm the presence of the elements in the precursor. The absence of other elements ensures their purity. The percentage of elements C, H, N, and metals (Co and Cu) present in the inorganic precursor was analyzed using Elemental analysis (CHN) and ICP-AES techniques. The analytical data of the precursor are found to be in good agreement with the proposed composition of the $[Co_{0.21}Cu_{0.79}(Cre)_2(N_2H_4)_2]$ inorganic precursor [Table 1].

5.1.2. FT-IR analysis

Investigation of FT-IR spectra of $[Co_{0.21}Cu_{0.79}(Cre)_2(N_2H_4)_2]$ inorganic precursor (Figure 1b) shows the occurrence of N-H stretching frequency at 3302 cm^{-1}. From the FT-IR spectra, the asymmetric and symmetric carbonyl stretching frequencies at 1613-1543 and 1411-1320 cm^{-1} shown by this precursor with an average separation of ($\Delta\nu = \nu_{asym} - \nu_{sym}$) of in the range of 202–223 cm^{-1} suggests the unidentate coordination of carboxylate ions to the metal ions. Thus, the creatinate anion coordinates to the metal as the unidentate ligand in the precursor. The N-N stretching frequency appears in the region

at 970 cm^{-1} attributes to the bridging bidentate nature of hydrazine moieties [27].

5.1.3. Thermogravimetry-differential thermal analyser (TG-DTA) analysis

From TG-DTA (Figure 1c), the inorganic precursor $[Co_{0.21}Cu_{0.79}(Cre)_2(N_2H_4)_2]$ undergoes total weight loss in a single step. The total weight loss of about 80% on the TG curve indicates that the precursor undergoes simultaneous dehydrazination and decarboxylation in a single step observed in the temperature range 180–300°C corresponding DTA peak show the sharp endotherm at 271°C to give fine powders of metal oxide as final residue. Thus, to analyze the products obtained from thermal decomposition of $[Co_{0.21}Cu_{0.79}(Cre)_2(N_2H_4)_2]$ inorganic precursor by FT-IR, Raman, XRD and XPS analysis, this sample was heated up to 300°C in a muffle furnace in the air atmosphere for 30 min.

Table 1: Analytical data of the $[Co_{0.21}Cu_{0.79}(Cre)_2(N_2H_4)_2]$ precursor

Analysis		$[Co_{0.21}Cu_{0.79}(Cre)_2(N_2H_4)_2]$		
1	Color	Brown	Observed	Calcuated
2	Hydrazine (%)		15.13	15.15
3	Elemental	C	22.66	22.69
	Analysis (%)	H	5.18	5.20
		N	33.07	33.09
4	Metal (%)	Co	2.85	2.92
	(ICP-AES)	Cu	11.84	11.86
5	Molecular mass (g)		422.9972	

Inductively Coupled Plasma Atomic Emission Spectrophotometry
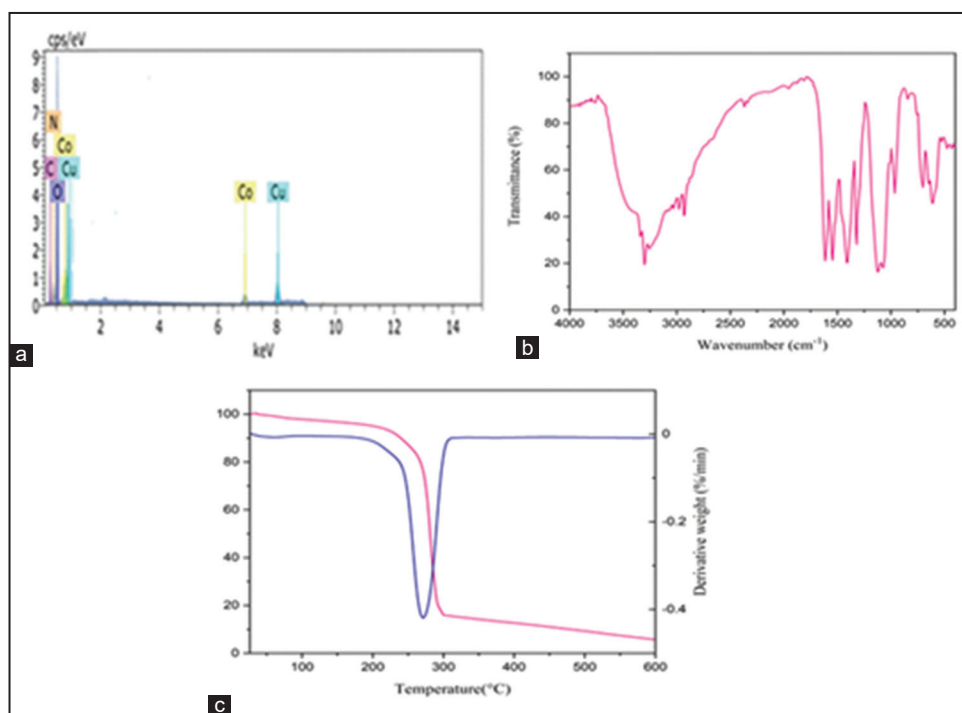
Figure 1: a. Energy dispersive X-ray spectroscopy spectrum, b. Fourier transform infrared spectrum and c. Thermogravimetry-differential thermal analyser of $[Co_{0.21}Cu_{0.79}(Cre)_2(N_2H_4)_2]$ precursor.

5.2. Characterization of $Co_{0.21}Cu_{0.79}O$ Nanoparticles

5.2.1. Elemental composition analysis
The presence of elements such as Co, Cu, and O in $Co_{0.21}Cu_{0.79}O$ nanoparticles has been analysed by EDS (Figure 2a) and their compositions have been identified using ICP-AES analysis. From these findings, no contamination element was detected [Table 2].

5.2.2. Structural analysis by X-ray diffraction
Figure 2b shows, the powder X-ray diffraction pattern of $Co_{0.21}Cu_{0.79}O$ nanoparticles recorded at room temperature. In XRD pattern, $Co_{0.21}Cu_{0.79}O$ nanoparticles show the diffraction peaks correspond to (1 1 0), (−1 1 1), (1 1 1), (−2 0 2), (0 2 0), (2 0 2), (−1 1 3), (−3 1 1),

(2 2 0), (3 1 1), and (−2 2 2) crystal planes of monoclinic CuO having C2/c space group (JCPDS card no 80–1916). Using the Unit cell program [5,28], in this work, we calculated the lattice parameters (a = 4.6919, b=3.4219, c=5.1358, and V = 81.3350) of $Co_{0.21}Cu_{0.79}O$ nanoparticles. Using the Debye-Scherrer formula, $D = K\lambda/\beta\cos\theta$, where θ is Bragg diffraction angle, K is Blank's constant, λ is the wavelength of X-ray radiation (1.54), and λ is the full width at half maximum (FWHM) of the peaks at the diffracting angle θ, the average crystallite size calculated was about 14.61 nm.

To estimate the effect of crystallite size (D) and strain (ε), we used a well-known Williamson-Hall (W-H) method which is given by the following relation, $\beta\cos\theta = (K\lambda/D) + 4\varepsilon\sin\theta$. The inset in Figure 2c

Table 2: ICP-AES data of $Co_{0.21}Cu_{0.79}O$ nanoparticles

| S.No	Sample	ICP-AES Analysis				Molecular mass (g)
		Co%		Cu%		
		Observed	Calculated	Observed	Calculated	
1	$Co_{0.21}Cu_{0.79}O$	15.72	15.75	63.83	63.88	78.5762

Inductively Coupled Plasma Atomic Emission Spectrophotometry
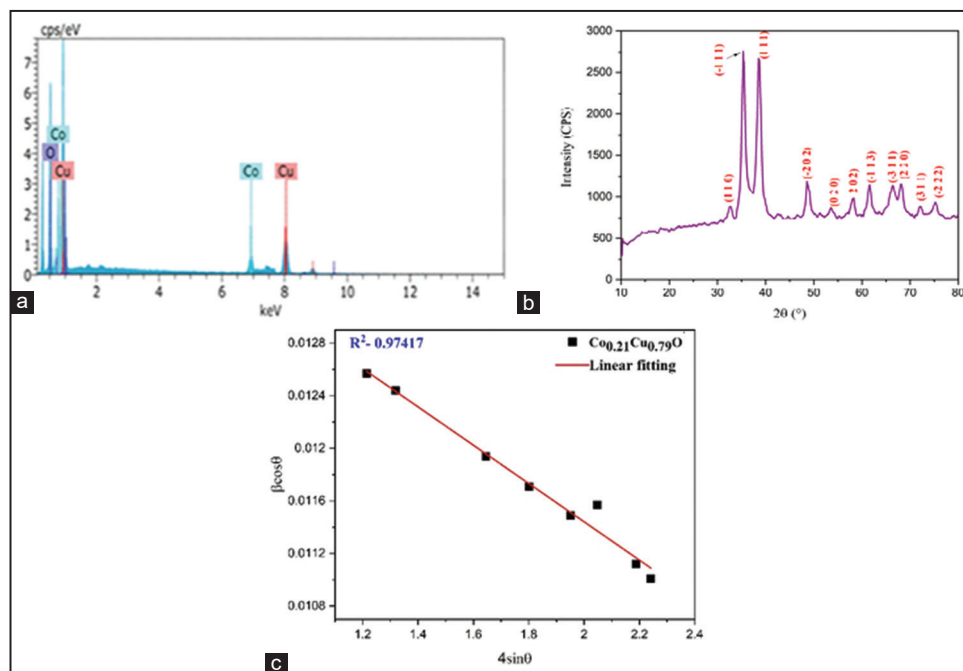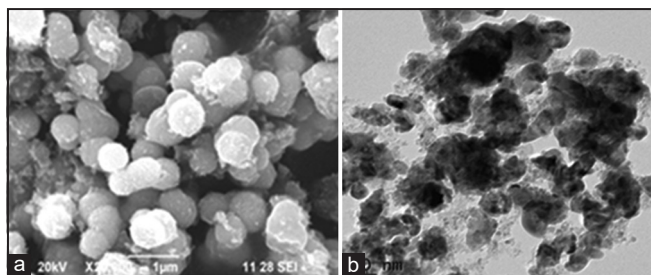

Figure 2: a. Energy dispersive X-ray spectroscopy, b. X-ray diffraction pattern and c. W-H plot of $Co_{0.21}Cu_{0.79}O$ nanoparticles.
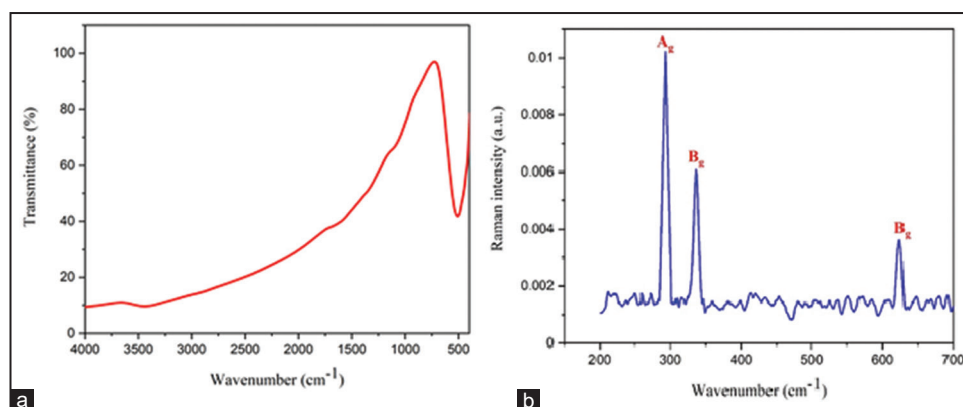
Figure 3: a. Fourier transform infrared and b. Raman spectra of $Co_{0.21}Cu_{0.79}O$ nanoparticles.
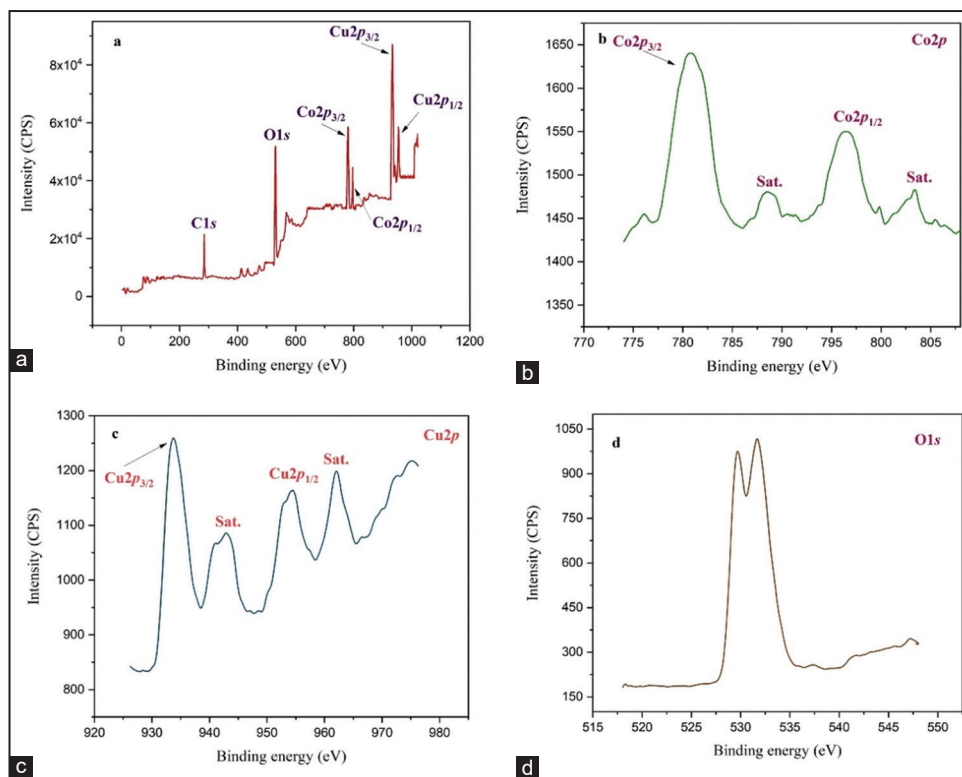
Figure 4: X-ray photoelectron spectroscopy spectra of $Co_{0.21}Cu_{0.79}O$ nanoparticles - a. wide scan, b. Co2p, c. Cu2p and d. O1s.

Figure 5: a. Scanning electron microscopy and b. Transmission electron microscope images of $Co_{0.21}Cu_{0.79}O$ nanoparticles.

shows the W-H plot of βcosθ versus 4sinθ. The intercept and slope of a linear fit in the W-H plot give the inverse of crystallite size and slope [29]. The negative slope of the linear fit in the W-H plot shows a compressive strain present in $Co_{0.21}Cu_{0.79}O$ and therefore the particle size obtained by Debye Scherrer (14.61 nm) formula is higher than that of the W-H plot (9.96 nm) for $Co_{0.21}Cu_{0.79}O$ nanoparticles indicating that the strain existing in the nanoparticles [29]. The dislocation density (δ) of $Co_{0.21}Cu_{0.79}O$ nanoparticles about 0.06402 was estimated using the formula, $δ= 1/D^2$ here D is the crystallite size for interpreting the defects in the nanoparticles [30]. The estimated dislocation density of $Co_{0.21}Cu_{0.79}O$ nanoparticles confirms the presence of defects.

5.2.3. FT-IR and Raman analysis

FT-IR spectra of $Co_{0.21}Cu_{0.79}O$ nanoparticles (Figure 3a) depict the presence of three distinctive vibrational modes. The band that appeared at 450 cm^{-1} is associated with A_u mode. The two characteristic bands in the range of 498 cm^{-1} and 548 cm^{-1} are related to two Bu modes. These three distinctive bands are attributed to the metal-oxygen (Cu-O) vibration, which confirms the monoclinic phase of CuO in $Co_{0.21}Cu_{0.79}O$ nanoparticles [31]. The Raman spectra of $Co_{0.21}Cu_{0.79}O$ nanoparticles are displayed in Figure 3b. This spectrum portrays

the presence of three well-known peaks at 281 cm^{-1} (A_g), 332 cm^{-1} (B_g), and 612 cm^{-1} (B_g), respectively, which are corresponds to the monoclinic phase of CuO as displayed in earlier reports [32]. Thus, the above results obtained from Raman spectroscopy are in good agreement with our previously reported results from FT-IR and XRD techniques, respectively.

5.2.4. XPS analysis

The survey spectra of $Co_{0.21}Cu_{0.79}O$ (Figure 4a) show the absence of impurities except for Co2p, Cu2p, O1s, and C1s. In Figure 4b, Co2p spectra exhibit two peaks at 780.90 and 796.36 eV are assigned to Co2$p_{3/2}$ and Co2$p_{1/2}$. The satellite peaks (788.42 and 803.32 eV) at higher binding energies are specifically connected with the +2 ionic state of Co. The peaks (Figure 4c) positioned at 934.08 and 954.46 eV are attributed to Cu2$p_{3/2}$ and Cu2$p_{1/2}$. The satellite peaks were observed at 943.26 and 962.60 eV, respectively, which confirms Cu^{2+} ions. The O1s core level spectra (Figure 4d) of $Co_{0.21}Cu_{0.79}O$ nanoparticles have two peaks. The peak located at 530.20 eV is assigned to the metal-oxygen bond, and the peak at 531.26 eV is attributed to oxygen defect/vacancies [33,34].

5.2.5. SEM and TEM analysis

SEM picture in Figure 5a shows the agglomeration of particles. TEM micrograph of $Co_{0.21}Cu_{0.79}O$ nanoparticles (Figure 5b) portrays spherical shape nanoparticles with the presence of agglomeration with the average particle size of 6–15 nm and proves good consistency between TEM and XRD results.

5.2.6. Textural analysis

The N_2 adsorption and desorption measurement was performed to determine the surface area of $Co_{0.21}Cu_{0.79}O$ nanoparticles. Figure 6a shows N_2 at 77 K adsorption and desorption isotherm which corresponds to Type IV isotherm and H3 hysteresis loop is in the range of (0.4–1.0) P/Po revealed the nature of $Co_{0.21}Cu_{0.79}O$ nanoparticles is mesoporous. The specific surface area for nanoparticles was calculated using the multi-point BET equation, which was 34.581 m^2/g. The
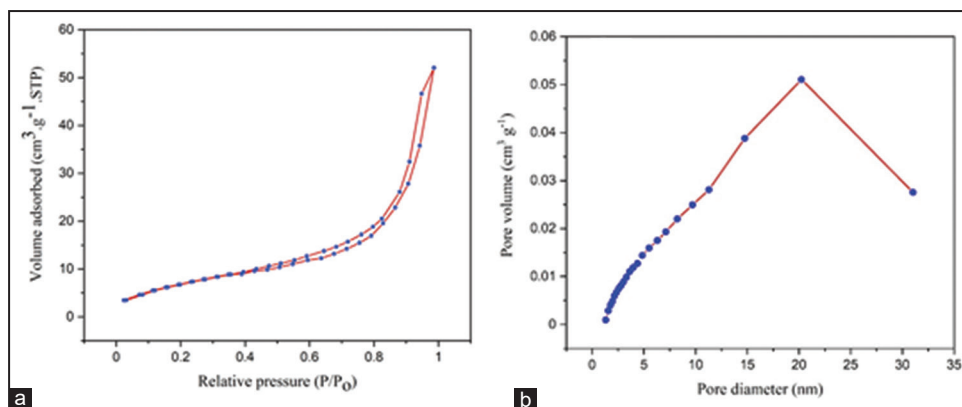
Figure 6: a. N_2 adsorption-desorption isotherm and b. BJH Pore Size Distribution (PSD) of $Co_{0.21}Cu_{0.79}O$ nanoparticles.
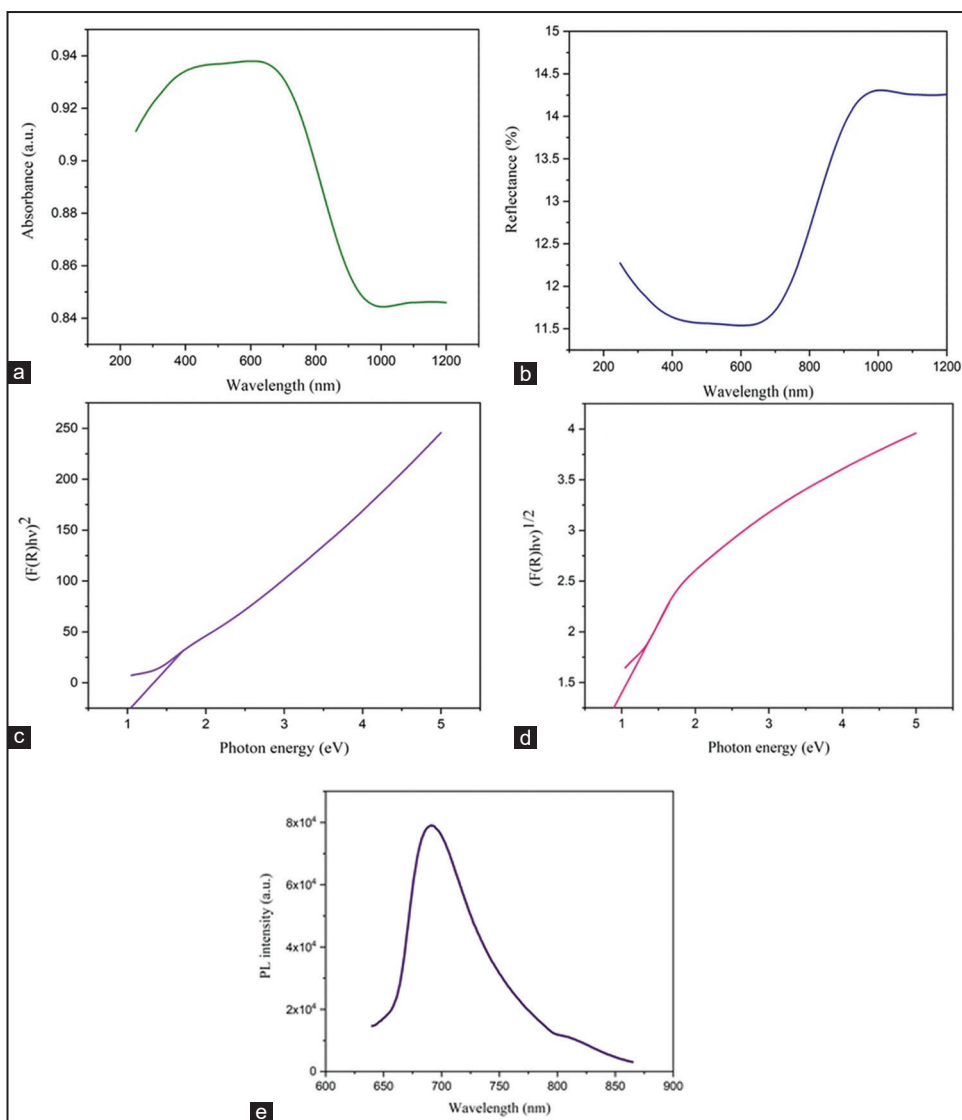
Figure 7: a. Absorbance and b. Reflectance, c. Direct band gap and d. Indirect band gap of $Co_{0.21}Cu_{0.79}O$ nanoparticles. e. PL spectra of $Co_{0.21}Cu_{0.79}O$ nanoparticles.

pore size distribution curve of nanoparticles has been drawn using the Barrett-Joyner-Halenda (BJH) method and shown in Figure 6b. From the BJH method, we can see that the pore volume was $0.051 cm^3/g$. Furthermore, the average pore diameter of $Co_{0.21}Cu_{0.79}O$ nanoparticles about 3.95 nm was estimated using the relation $D_p = 4V_{BJH}/S_{BJH}$,

where V_{BJH} = pore volume (cm^3/g) and S_{BJH} = surface area of pores (m^2/g) [35].

5.2.7. Optical properties
Figure 7a and b show that the absorption and reflectance behavior of $Co_{0.21}Cu_{0.79}O$ nanoparticles were measured with a UV-Vis-NIR

and UV-DRS spectrophotometer. It can be seen that nanoparticles exhibit maximum absorption at 650 nm. To calculate the direct and

indirect band gap values for nanoparticles from the reflectance spectrum (Figure 7b), we used the tauc's relation, $F(R)h\nu = A(h\nu-E_g)^n$, Where $F(R)$ is the Kubelka Munk function which is proportional to the absorbance coefficient (α) and calculated using the relation $F(R) = (1-R)^2/2R$, Where A is constant, $h\nu$ is photon energy, and the co-efficient n is either 2 for direct transition or ½ (0.5) for an indirect transition [36-38]. The tauc's plot of direct band variation of $(F(R)h\nu)^2$ and indirect band variation of $(F(R)h\nu)^{1/2}$ against photon energy (eV) for $Co_{0.21}Cu_{0.79}O$ nanoparticles are shown in Figure 7c and d. The direct (E_g) and indirect band gap energy (E_g) were obtained by extrapolating the linear portion of the plot to the photon energy $h\nu$ axis. The calculated direct and indirect band and gaps for $Co_{0.21}Cu_{0.79}O$ nanoparticles are 1.04 eV and 0.85 eV, respectively.
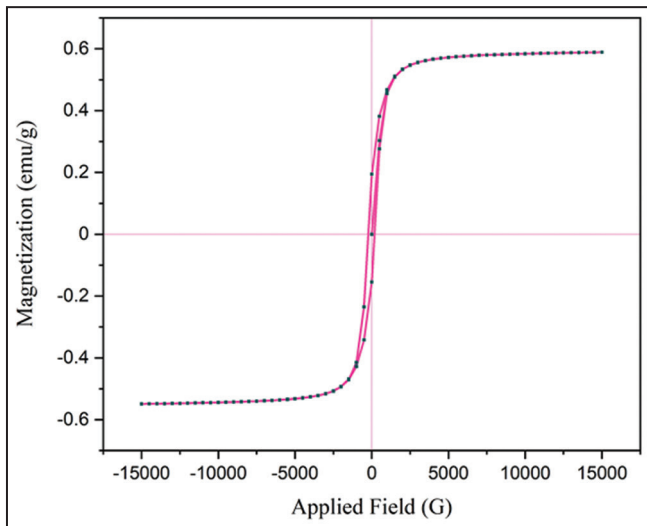
5.2.8. PL analysis

The PL spectra give direct information about the defect present in the materials. The room temperature PL spectra of $Co_{0.21}Cu_{0.79}O$ nanoparticles (excited at 650 nm) are shown in Figure 7e. The red emission band of the luminescent peak at 690 nm arose due to the presence of defects [39].

5.2.9. Magnetic studies

Figure 8 portrays the magnetic hysteresis (M-H) loop of $Co_{0.21}Cu_{0.79}O$ nanoparticles taken at room temperature with an applied magnetic

Figure 8: Magnetization (m) *vs.* applied field (h) plot of $Co_{0.21}Cu_{0.79}O$ nanoparticles.
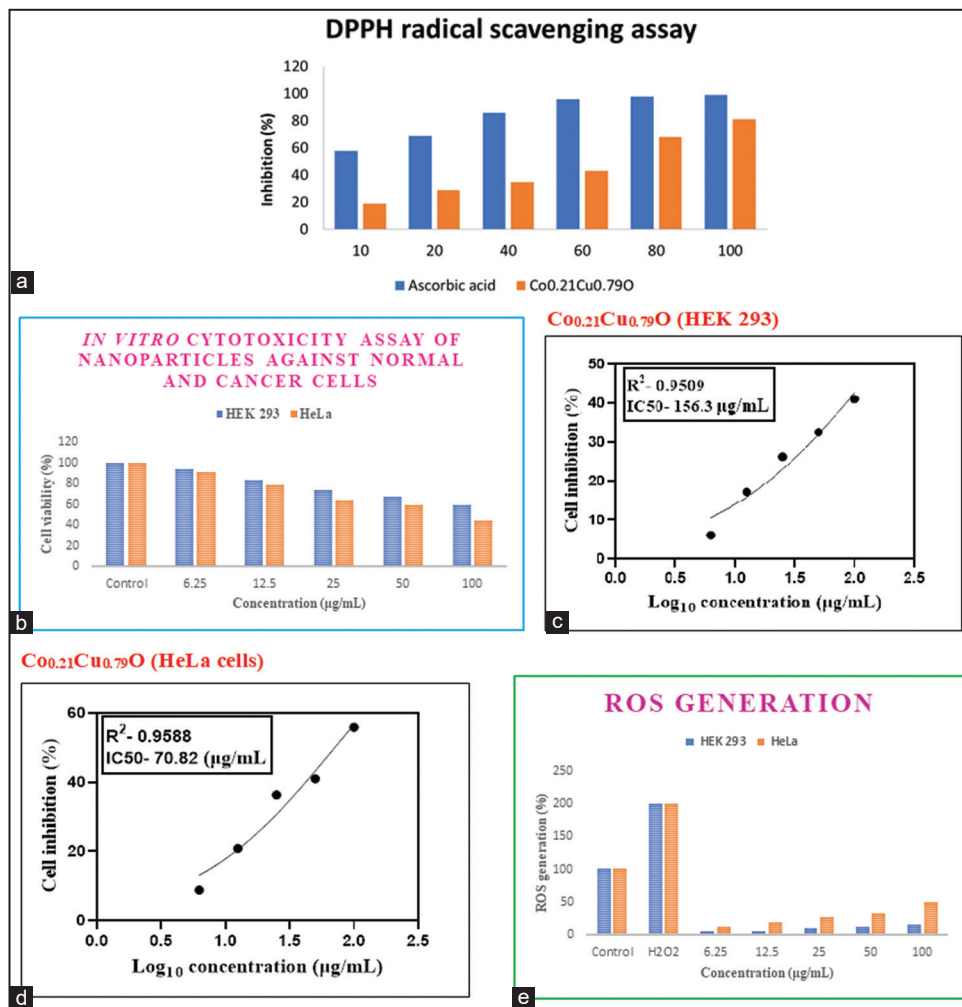
Figure 9: a. *In vitro* antioxidant activity (DPPH scavenging) of $Co_{0.21}Cu_{0.79}O$ nanoparticles. b. Effect of $Co_{0.21}Cu_{0.79}O$ nanoparticles on the viability of HEK 293 and HeLa cell lines, c. and d. the nonlinear regression plot between % Cell inhibition and Log_{10} concentration of $Co_{0.21}Cu_{0.79}O$ nanoparticles against HEK 293 (normal) and HeLa (cancer) cells and e. ROS generation of $Co_{0.21}Cu_{0.79}O$ nanoparticles against HEK 293 (normal) and HeLa (cancer) cells.

field in the range of ±15,000 Oe. The magnetic parameters such as saturation magnetization (M_s-0.5946 emu.g^{-1}), retentivity magnetization (M_r-0.1860emu.g^{-1}), coercivity (H_c-210.99 Oe), and squareness (M_r/M_s-0.3128) were observed. From the above results, the observed low values for magnetic parameters such as M_s, H_c, M_r, and M_r/M_s reveal the occurrence of weak ferromagnetism in $Co_{0.21}Cu_{0.79}O$ nanoparticles. Furthermore, other parameters like the anisotropy constant (K_a) value of about 128.0149 can be calculated using $K_a=H_c*M_s/0.98$ and the magnetic moment (μ_m) of about 0.0083 can be calculated using $\mu_m = M_s*M_w/5585$ where M_w is the molecular weight.

5.3. Biological Applications

5.3.1. In vitro antioxidant activity (DPPH assay) of nanoparticles

Figure 9a displays, the DPPH free-radical scavenging ability of $Co_{0.21}Cu_{0.79}O$ nanoparticles with ascorbic acid as standard. The percentage of antioxidant activity of nanoparticles was assessed by DPPH free-radical assay in a dose-dependent manner, as the concentration of $Co_{0.21}Cu_{0.79}O$ nanoparticles increases, the DPPH scavenging activity also increased (Figure 9). However, on comparing the DPPH scavenging activity with standard ascorbic acid, the $Co_{0.21}Cu_{0.79}O$ nanoparticles exhibit moderate scavenging activity. Furthermore, the calculated IC50 value for $Co_{0.21}Cu_{0.79}O$ nanoparticles (52.86 μg/ml) was higher than standard ascorbic acid (22.06 μg/ml) [40]. This result suggests that the $Co_{0.21}Cu_{0.79}O$ nanoparticles have a moderate potential that can be used in cytotoxicity and hence in medical treatment.

5.3.2. In vitro cytotoxicity assay and ROS generation of $Co_{0.21}Cu_{0.79}O$ nanoparticles

The cytotoxicity of the $Co_{0.21}Cu_{0.79}O$ nanoparticles has been investigated against HEK 293 and HeLa cell lines via MTT assay. HeLa and HEK 293 cell inhibited were evaluated after 48 h exposure to nanoparticles of various concentrations ranging from 6.25 μg/ml to 100 μg/ml. Controlled samples, that is, untreated samples are also provided for comparison. It has been observed from Figure 9b, the % cell viability of the nanoparticles toward cancer and normal cell lines. Figure 9c and d show the non-linear regression graph plotted between % Cell inhibition and Log concentration. IC50 was determined using Graph Pad Prism software. Furthermore, the as-synthesized nanoparticles have inhibited the normal and cancer cell viability of about 51% and 100% at 100μg/ml concentration. Thus, $Co_{0.21}Cu_{0.79}O$ nanoparticles induced cytotoxicity on HEK 293 and HeLa cell were found to be increasing with an increase in concentration from 6.25 μg/ml to 100 μg/ml. Furthermore, Figure 9b proves that the $Co_{0.21}Cu_{0.79}O$ nanoparticles exhibited less cytotoxicity against normal cell than cancer cells. The IC50 values of nanoparticles against HEK 293 and HeLa cells were found to be 156.3 μg/ml and 70.82 μg/ml, respectively, after 48 h of exposure. This behavior of $Co_{0.21}Cu_{0.79}O$ nanoparticles reveals their dosage-dependent manner. As mentioned in earlier reports, ROS generation plays an important role in the cytotoxicity mechanism. To confirm whether the dose-dependent cytotoxicity of the synthesized $Co_{0.21}Cu_{0.79}O$ nanoparticles may be attributed to the ROS production or not, a ROS generation study was performed. In this study, we have experimentally investigated the ROS generation caused by nanoparticles both in normal and cancer cells. Figure 9e depicts a high level of ROS generation in the case of cancerous cells as compared with normal cells which are also observed to increase with the increase in concentration. It is confirmed that the dose-dependent cytotoxicity of synthesized nanoparticles is due to ROS generation. Hence, more work needs to be done in this regard and we are working on it.

6. CONCLUSION

At last, we have successfully synthesized $Co_{0.21}Cu_{0.79}O$ nanoparticles using the co-precipitation method followed by thermal decomposition of the hydrazine precursor to examining its structural, chemical state, textural, optical, and magnetic properties. XRD pattern of $Co_{0.21}Cu_{0.79}O$ nanoparticles was indexed to a monoclinic structure which coincides with IR and Raman results. XPS study confirmed the oxidation state of metals in $Co_{0.21}Cu_{0.79}O$ nanoparticles. The band gap of as-synthesized nanoparticles has been determined using tauc's plot. PL, XRD, and magnetic studies confirmed the presence of defects. Room temperature ferromagnetism was observed. Furthermore, $Co_{0.21}Cu_{0.79}O$ nanoparticles possessed moderate antioxidant potential and dose-dependent cytotoxicity against normal and cancerous cells. These findings may open new insight into cancer therapy by nanomedicines in near future. Hence, a great amount of work is still needed to do in this regard.

7. DISCLOSURE STATEMENT

No potential conflict of interest was reported by the authors.

8. ACKNOWLEDGMENT

9. REFERENCES

1. S. P. Kamble, V. D. Mote, (2019) Structural, optical and magnetic properties of Co-doped CuO nanoparticles by sol-gel auto combustion technique, **Solid State Sciences**, **95:** 105936.

2. S. Srivastava, A. Agarwal, (2018) Influence of Co doping on structural and optical properties of CuO nanoparticles, **Journal of Ovonic Research**, **14:** 395-404.

3. N. Thakur, Anu, K. Kumar, (2020) Effect of (Ag, Co) co-doping on the structural and antibacterial efficiency of CuO nanoparticles: A rapid microwave-assisted method, **Journal of Environmental Chemical Engineering**, **8:** 104011.

4. N. M. Basith, J. J. Vijaya, L. J. Kennedy, M. Bououdina, S. Hussain, (2014) Optical and magnetic properties of Co-coped CuO flower/plates/particles-like nanostructures, **Journal of Nanoscience and Nanotechnology**, **14:** 2577-2583.

5. V. Ponnarasan, A. Krishnan, (2016) Synthesis, structural and optical properties of cobalt doped CuO nanoparticles, **International Journal of Nanoscience**, **15:** 1650031.

6. R. V. Vijayalakshmi, G. Saravanan, P. P. Kumar, K. Ravichandran, (2018) Systematic analysis of CuO and Co-doped CuO nanoparticles and the impact of dopant on magnetic and optical properties, **AIP Conference Proceedings**, **1953:** 030160.

7. A. Pramothkumar, N. Senthilkumar, K. C. M. Gnana Malar, M. Meena, I. V. Potheher, (2019) comparative analysis on the dye degradation efficiency of pure, Co, Ni and Mndoped CuO nanoparticles, **Journal of Materials Science: Materials in Electronics**, **30:** 19043-19059.

8. B. P. Singh, M. Chaudhary, A. Kumar, A. K. Singh, Y. K. Gautam, S. Rani, R. Walia, (2020) Effect of Co and Mn doping on the morphological, optical and magnetic properties of CuO

nanostructures, *Solid State Sciences*, **106:** 106296.

9. Anu, N. Thakur, K. Kumar, K. K. Sharma, (2020) Application of Co-doped copper oxide nanoparticles against different multidrug resistance bacteria, *Inorganic and Nano-Metal Chemistry*, **50: 933-943.

10. K. Kalpanadevi, C. R. Sinduja, R. Manimekalai, (2013) Characterization of $ZnFe_2O_4$ nanoparticles obtained by the thermal decomposition of $ZnFe_2(cin)_3(N_2H_4)_3$, *Acta Chimica Slovenica*, **60:** 896-900.

11. K. Kalpanadevi, C. R. Sinduja, R. Manimekalai, (2014) A facile thermal decomposition route to synthesise $CoFe_2O_4$ nanostructures, *Materials Science-Poland*, **32:** 2014, 34-38.

12. K. Kalpanadevi, C. R. Sinduja, R. Manimekalai, (2014) Synthesis and structural studies of nanocrystalline $Cd_{0.3}Zn_{0.7}Fe_2O_4$, *South African Journal of Chemistry*, **67:** 91-93.

13. K. Kalpanadevi, C. R. Sinduja, R. Manimekalai, (2014) Characterisation of nanostructured Co_3O_4 synthesised by the thermal decomposition of an inorganic precursor, *Australian Journal of Chemistry*, **67:** 1671-1674.

14. K. Kalpanadevi, C. R. Sinduja, R. Manimekalai, (2016) Synthesis and characterisation of $Ni_{0.25}Co_{0.75}Fe_2O_4$ nanostructure, *Bulletin of the Chemical Society of Ethiopia*, **30:** 79-85.

15. C. R. Sinduja, K. Kalpanadevi, R. Manimekalai, (2015) Preparation and characterization of $Mn_{0.5}Zn_{0.5}Fe_2(PhAc)_3(N_2H_4)_2$: A new precursor to $Mn_{0.5}Zn_{0.5}Fe_2O_4$ nanoparticles, *Synthesis and Reactivity in Inorganic, Metal-Organic, and Nano-Metal Chemistry*, **45:** 482-486.

16. C. R. Sinduja, K. Kalpanadevi, R. Manimekalai, (2016) Preparation and characterization of $Co_{0.8}Zn_{0.2}Fe_2(PhAc)_3(N_2H_4)_3$: A new precursor to $Co_{0.8}Zn_{0.2}Fe_2O_4$ nanoparticles, *Materials Science (Medžiagotyra)*, **22:** 3-6.

17. N. Anjuthaprabha, R. Manimekalai, (2019) Synthesis, textural and magnetic properties of doped and undoped CuO nanoparticles, *Journal of Coordination Chemistry*, **72:** 83-101.

18. O. Raina and R. Manimekalai, (2018) Photocatalysis of cobalt zinc ferrite nanorods under solarlight, *Research on Chemical Intermediates*, **44:** 5941-5951.

19. S. Hemamalini, R. Manimekalai, (2020) Synthesis, structural, magnetic, textural, optical investigation and photocatalytic performance of undoped and doped cobaltite nanoparticles, *Journal of Coordination Chemistry*, **73:** 3431-3451.

20. K. Vasuki, R. Manimekalai, (2019) NIR light active ternary modified ZnO nanocomposites for combined cancer therapy, *Heliyon*, **5**: e02729.

21. M. N. Alam, N. J. Bristi, M. Rafiquzzaman, (2013) Review on *in vivo* and *in vitro* methods evaluation of antioxidant activity, *Saudi Pharmaceutical Journal*, **21:** 143-152.

22. A. Serpen, E. Capuano, V. Fogliano, V. Gökmen, (2007) A New procedure to measure the antioxidant activity of insoluble food components, *Journal of Agricultural Food Chemistry*, **55:** 7676-7681.

23. T. Mosmann, (1983) Rapid colorimetric assay for cellular growth and survival: Application to proliferation and cytotoxicity assays, *Journal of Immunological Methods*, **65:** 55-63.

24. A. Monks, D. Scudiero, P. Skehan, R. Shoemaker, K. Paull, D. Vistica, C. Hose, J. Langley, P. Cronise, W. A. Vaigro, G. M. Gray, H. Campbell, J. Mayo, M. Boyd, (1991) Feasibility of high flux anticancer drug screen using a diverse panel of cultured human tumour cell lines, *Journal of the National Cancer Institute*, **83:** 757-766.

25. A. Abruzzo, G. Zuccheri, F. Belluti, S. Provenzano, L. Verardi,

F. Bigucci, T. Cerchiara, B. Luppi, N. Calonghi, (2016) Chitosan nanoparticles for lipophilic anticancer drug delivery: Development, characterization and *in vitro* studies on HT29 cancer cells, *Colloids Surfaces. B, Biointerfaces*, **145:** 362-372.

26. Vogel, (1986) *A Textbook of Quantitative Inorganic Analysis*, London: Longman.

27. C. Patil and T. M. Rattan, (2014) *Inorganic Hydrazine Derivatives: Synthesis, Properties and Applications*, Chichester: John Wiley and Sons, Inc.

28. T. J. B. Holland, (1997) Unit cell refinement from powder diffraction data: The use of regression diagnostics, *Mineralogical Magazine*, **61:** 65-77.

29. G. R. Santhakumari, S. J. K. Vethanathan, and K. U. Madhu, (2020) Enhancement of structural, optical and electrical properties of manganese doped stannic oxide nanoparticles, *Journal of Scientific Research*, **64:** 267-273.

30. M. M. Obeid, H. R. Jappor, K. Al-Marzoki, I. A. Al-Hydary, S. J. Edrees, M. M. Shukur, (2019) Unraveling the effect of Gd doping on the structural, optical and magnetic properties of ZnO based diluted magnetic semiconductor nanorods, *RSC Advances*, **9:** 33207-33221.

31. A. Pramothkumar, N. Senthilkumar, K. C. M. Gnana Malar, M. Meena, I. Vetha Potheher, (2019) A comparative analysis on the dye degradation eficiency of pure, Co, Ni and Mn-doped CuO nanoparticles, *Journal of Materials Science: Materials in Electronics*, **30:** 19043-19059.

32. H. Hagemann, H. Bill, W. Sadowski, E. Walker, M. Francois, (1990) Raman spectra of single crystal CuO, *Solid State Communications*, **73:** 447-451.

33. S. Ramya, G. Viruthagiri, R. Gobi, N. Shanmugam, N. Kannadasan, (2016) Synthesis and characterization of Ni^{2+} ions incorporated CuO nanoparticles and its application in antibacterial activity, *Journal of Materials Science: Materials in Electronics*, **27:** 2701-2711.

34. H. Zhang, J. Wang, Y. Cao, X. Guo, Q. Li, J. Du, Q. Xu, (2018) Oxygen vacancies mediated ferromagnetism in hydrogenated $Zn_{0.9}Co_{0.1}O$ film, *AIP Advances*, **8:** 056405.

35. C. Herdes, M. A. Santos, F. Medina, L. F. Vega, (2005) Pore size distribution analysis of selected hexagonal mesoporous silicas by grand canonical monte carlo simulations, *Langmuir*, **21:** 8733-8742.

36. A. Somvanshi, S. Husain, W. Khan, (2019) Investigation of structure and physical properties of cobalt doped nano-crystalline neodymium orthoferrite, *Journal of Alloys Compounds*, **778:** 439-451.

37. R. Remya, M. A. Khadar, (2018) Structural, optical and electrical properties of Cu doped α-Fe O nanoparticles, *Materials Chemistry and Physics*, **219:** 142-154.

38. P. Malkeshkumar, C. Arvind, M. Indrajit, K. Joondong, R. Abhijit, (2015) Nanostructured SnS with inherent anisotropic optical properties for high photoactivity, *Nanoscale*, **8:** 2293-2303.

39. I. A. Zgair, A. H. O. Alkhayatt, A. A. Muhmood, S. K. Hussain, (2019) Investigation of structure, optical and photoluminescence characteristics of Li doped CuO nanostructure thin films synthesized by SILAR method, *Optik-International Journal for Light and Electron Optics*, **191**, 48-54.

40. D. D. Purkayastha, N. Das, C. R. Bhattacharjee, (2014) Synthesis and antioxidant activity of cupric oxide nanoparticles accessed via low-temperature solid state thermal decomposition of bis(dimethylglyoximato)copper(II) complex, *Materials Letters*, **123:** 206-209.